The Discontinuous Galerkin Finite-Element Time-Domain Method Solution of Maxwell's Equations

Stephen D. Gedney [1], Chong Luo [1], J. Alan Roden [2], Robert D. Crawford [2], Bryan Guernsey [2], Jeffrey A. Miller [2], Tyler Kramer [2], and Eric W. Lucas [3]

[1] Department of Electrical and Computer Engineering
Univ. of Kentucky, Lexington, KY, 40506-0046 USA
gedney@engr.uky.edu, cluo01@engr.uky.edu

[2] The Aerospace Corporation,Chantilly, VA
JAlan.Roden@aero.org, Robert.D.Crawford@aero.org, Bryan.J.Guernsey@aero.org, Jeffrey.A.Miller@aero.org, Tyler.C.Kramer@aero.org

[3] Alpha Omega Electromagnetics, LLC, Ellicott City, MD
alphaomega@maranatha.net

***Abstract*—** A Discontinuous Finite-Element Time-Domain method is presented that is based on a high-order finite element discretization of Maxwell's curl equations. The problem domain is decomposed into non-overlapping subdomains that couple through boundary integral terms. Within each subdomain, the tangential electric and magnetic fields are discretized via high-order curl conforming basis functions, leading to a high-order representation of the volume fields. For unbounded problems, a perfectly matched layer absorbing medium is used. The discrete equations are presented in a symmetric form. The method leads to an explicit time-dependent solution of Maxwell's equations that is high-order convergent.

***Index Terms*—** Discontinuous Galerkin Method, Finite-Element Time-Domain.

I. INTRODUCTION

Discontinuous Galerkin Time-Domain methods are a class of finite element methods that employ piecewise continuous basis and testing functions. The methods are characterized as being high-order accurate, able to model complex geometries, efficient, stable, and highly parallel [1]. Discontinuous Galerkin Time-Domain (DGTD) methods have more recently been employed for the solution of Maxwell's equations [2-8]. DGTD methods are typically based on a point-based discretization by sampling at Gauss-Lobatto Quadrature points. The fields are interpolated by a polynomial expansion over each cell, which are then projected onto the quadrature points [1, 4]. One can thus draw an analog between DGTD methods and point-based Nyström discretizations used for integral equation solutions [9, 10]. DGTD methods have proven to be highly accurate, providing exponential convergence and have provided an excellent solution method for large scale electromagnetic simulations. [2-8].

It is noted that the vector fields of DGTD methods are projected onto a polynomial complete function space. A concern arises that near discontinuities or geometric singularities spurious charges can corrupt the solution. Thus, penalty methods have been recommended to weakly enforce the divergence preserving properties of the fields [11]. Furthermore, for late-time stability, upwind flux methods have also been recommended [4, 5].

In this paper, a Discontinuous Galerkin method based on a finite-element discretization is presented. This method, which is referred to as the Discontinuous Galerkin Finite-Element Time-Domain (DGFETD) method, is based on a finite-element discretization of Maxwell's curl equations [12]. Rather than a point-based sampling, both the electric and magnetic fields are expanded via hierarchical Nedelec curl-conforming mixed-order basis functions [13, 14]. Similar to the DGTD method, tangential field continuity is weakly constrained across shared boundaries. Due to the properties of curl-conforming vector basis functions, only basis functions associated with

topologies on a domain boundary (i.e., edges and faces) have a non-zero tangential projection. Thus, only local basis functions are shared across domain boundaries. This is similar to DGTD methods. The use of curl-conforming basis functions that satisfy Nedelec's criterion also avoids the concern of spurious solutions [15]. Hence, the formulation avoids the need for penalty methods [16]. Furthermore, the method does not require upwind flux terms for stability. The use of hierarchal curl-conforming basis functions allows for local *hp*-refinement of the discretization. Another advantage of the DGFETD formulation is that sub-domains are not restricted to single cells. Rather, an arbitrary partitioning of the domain can be employed.

Other finite-element time-domain discretizations of Maxwell's curl equations have been proposed [17-20]. The majority of these methods provide a reciprocal discretization based on a curl-conforming basis function representation for the electric field intensity, and a divergence conforming basis function representation of the magnetic flux density (or the dual H-D formulation). Time domain integration is typically performed using Symplectic time-integration methods. In contrast, the proposed DGFETD scheme expands both the electric and magnetic field intensities using high-order curl-conforming basis functions. Also, high-order Runge-Kutta time-integration methods are employed. The proposed DGFETD method thus provides an explicit solution scheme that is high-order in both space and time leading to exponential convergence

A salient feature of the proposed DGFETD formulation is that a PML termination is naturally represented. The perfectly matched quality of a PML medium is based on a dual behavior of the electric and magnetic properties of the material media. This is ideally represented by the proposed formulation, which has dual function space representations for the field intensities, and the flux densities. The time-integration scheme also assumes that the electric and magnetic fields are co-located in time. As a consequence, it is found that the PML implementation within the DGFETD scheme provides upwards to 5 digits of accuracy with only a 2 cell thick PML that has a constant material profile. In this paper, the DGFETD formulation and discretization are presented in Sections II – IV. The implementation of a perfectly matched layer absorbing medium for simulating unbounded domains is presented in Section V. A number of numerical simulations based on the DGFETD scheme are presented in Section VI. Through these examples, the exponential convergence of the DGFETD method is demonstrated, and the performance of the PML is validated.

II. THEORY

Consider the electromagnetic fields that are radiated by electric or magnetic current densities in a domain Ω bound by $\partial\Omega$. The fields must satisfy Maxwell's curl equations:

$$\nabla\times\vec{E} = -\frac{\partial}{\partial t}\bar{\bar{\mu}}\cdot\vec{H} - \bar{\bar{\sigma}}^{*}\cdot\vec{H} - \vec{M}\,, \tag{1}$$

$$\nabla\times\vec{H} = \frac{\partial}{\partial t}\bar{\bar{\varepsilon}}\cdot\vec{E} + \bar{\bar{\sigma}}\cdot\vec{E} + \vec{J}\,, \tag{2}$$

where, $\bar{\bar{\mu}}$, $\bar{\bar{\varepsilon}}$, $\bar{\bar{\sigma}}^{*}$, and $\bar{\bar{\sigma}}$ are permeability, permittivity, and conductivity tensors, and $\vec{J}$ and $\vec{M}$ are impressed current densities.

The domain Ω is subdivided into non-overlapping and contiguous subdomains. The i^{th} subdomain is defined by the volume V_i and bound by ∂V_i. Each subdomain is then discretized with fitted polyhedra, or finite elements. The field intensities are expanded within each finite element using suitable vector basis functions weighted by time-dependent coefficients. A set of testing functions that span the same function space as the basis functions is also introduced. The inner product of the coupled curl equations with a set of test functions is performed:

$$\int_{V_i}\vec{T}^{h}\cdot\left[\frac{\partial}{\partial t}\bar{\bar{\mu}}\cdot\vec{H} + \bar{\bar{\sigma}}^{*}\cdot\vec{H} + \vec{M} + \nabla\times\vec{E}\right]dv = 0\,, \tag{3}$$

$$\int_{V_i}\vec{T}^{e}\cdot\left[\frac{\partial}{\partial t}\bar{\bar{\varepsilon}}\cdot\vec{E} + \bar{\bar{\sigma}}\cdot\vec{E} + \vec{J} - \nabla\times\vec{H}\right]dv = 0\,, \tag{4}$$

where $\vec{T}^{h}$ and $\vec{T}^{e}$ are testing functions that span the $\vec{H}$ and $\vec{E}$ -field function spaces, respectively. After applying a vector identity, the curl term in (3) can be written as:

$$\int_{V_i}\vec{T}^{h}\cdot\nabla\times\vec{E}dv = \int_{V_i}\vec{E}\cdot\nabla\times\vec{T}^{h}dv + \oint_{\partial V_i}\vec{T}^{h}\cdot\left(\hat{n}\times\vec{E}\right)ds\,, \tag{5}$$

where $\hat{n}$ is the outward normal of ∂V_i. It is assumed that the tangential field $\hat{n}\times\vec{E}$ on ∂V_i is the field just interior to V. Let $\hat{n}\times\vec{E}^{+}$ represent the tangential field on ∂V_i just exterior to V_i. The exterior field is typically the field of a neighboring subdomain. For generality, assume there is an impressed magnetic surface current density on ∂V_i. Consequently, the tangential electric fields must satisfy the relationship:

$$\hat{n}\times\left(\vec{E} - \vec{E}^{+}\right)\Big|_{\partial V_i} = -\vec{M}_s\,, \tag{6}$$

where, $\hat{n}$ is to be the outward normal to V_i. This boundary condition can be rewritten as:

$$2\hat{n}\times\vec{E}\Big|_{\partial V_i} = \left(\hat{n}\times\vec{E}^{+} + \hat{n}\times\vec{E}\right)\Big|_{\partial V_i} - \vec{M}_s, \quad (7)$$

$$\text{or,}\quad \hat{n}\times\vec{E}\Big|_{\partial V_i} = \frac{1}{2}\left(\hat{n}\times\vec{E} + \hat{n}\times\vec{E}^{+}\right)\Big|_{\partial V_i} - \frac{1}{2}\vec{M}_s, \quad (8)$$

which is equivalent to averaging the tangential fields. Substituting this into (5) leads to:

$$\int_{V_i}\vec{T}^h\cdot\nabla\times\vec{E}dv = \int_{V_i}\vec{E}\cdot\nabla\times\vec{T}^h dv + \frac{1}{2}\oint_{\partial V_i}\vec{T}^h\cdot\left(\hat{n}\times\vec{E} + \hat{n}\times\vec{E}^{+}\right)ds - \frac{1}{2}\oint_{\partial V_i}\vec{T}^h\cdot\vec{M}_s ds. \quad (9)$$

Next, from (5)

$$\frac{1}{2}\oint_{\partial V_i}\vec{T}^h\cdot\hat{n}\times\vec{E}ds = \frac{1}{2}\int_{V_i}\vec{T}^h\cdot\nabla\times\vec{E}dv - \frac{1}{2}\int_{V_i}\vec{E}\cdot\nabla\times\vec{T}^h dv. \quad (10)$$

This is combined with (9), leading to:

$$\int_{V_i}\vec{T}^h\cdot\nabla\times\vec{E}dv = \frac{1}{2}\int_{V_i}\vec{T}^h\cdot\nabla\times\vec{E}dv + \frac{1}{2}\int_{V_i}\vec{E}\cdot\nabla\times\vec{T}^h dv + \frac{1}{2}\oint_{\partial V_i}\vec{T}\cdot\hat{n}\times\vec{E}^{+}ds - \frac{1}{2}\oint_{\partial V_i}\vec{T}^h\cdot\vec{M}_s ds. \quad (11)$$

Finally, applying (11) within (3) leads to the operator:

$$\int_{V_i}\left[\begin{array}{l}\dfrac{\partial}{\partial t}\vec{T}^h\cdot\bar{\bar{\mu}}\cdot\vec{H} + \vec{T}^h\cdot\bar{\bar{\sigma}}^{*}\cdot\vec{H} + \vec{T}^h\cdot\vec{M}_V \\ +\dfrac{1}{2}\vec{T}^h\cdot\nabla\times\vec{E} + \dfrac{1}{2}\vec{E}\cdot\nabla\times\vec{T}^h\end{array}\right]dv = -\frac{1}{2}\oint_{\partial V_i}\vec{T}^h\cdot\hat{n}\times\vec{E}^{+}ds + \frac{1}{2}\oint_{\partial V_i}\vec{T}^h\cdot\vec{M}_s ds. \quad (12)$$

By duality, (4) can also be written as:

$$\int_{V_i}\left[\begin{array}{l}\dfrac{\partial}{\partial t}\vec{T}^e\cdot\bar{\bar{\varepsilon}}\cdot\vec{E} + \vec{T}^e\cdot\bar{\bar{\sigma}}\cdot\vec{E} + \vec{T}^e\cdot\vec{J}_V \\ -\dfrac{1}{2}\vec{T}^e\cdot\nabla\times\vec{H} - \dfrac{1}{2}\vec{H}\cdot\nabla\times\vec{T}^e\end{array}\right]dv = \frac{1}{2}\oint_{\partial V_i}\vec{T}^e\cdot\hat{n}\times\vec{H}^{+}ds + \frac{1}{2}\oint_{\partial V_i}\vec{T}^e\cdot\vec{J}_s ds, \quad (13)$$

where, $\vec{J}_s$ is an impressed surface current density, and $\vec{H}^{+}$ is the magnetic field exterior to V_i on ∂V_i.

Equations (12) and (13) represent the weak form of Maxwell's curl equations that will be applied within each sub-domain. The fields $\vec{E}$ and $\vec{H}$ are associated uniquely with subdomain V_i. Each subdomain is coupled with neighboring sub-domains, or an exterior region, through the boundary integral terms. It is noted that the surface current densities are zero unless an impressed current density is placed on the boundary. Hence, the boundary integral terms weakly constrain the continuity of the tangential fields across source-free sub-domain boundaries.

III. DISCRETIZATION

Each subdomain is discretized with a fitted polyhedral mesh, which can be hexahedron, tetrahedron, or prisms. Within each sub-domain, the field intensities $\vec{E}$ and $\vec{H}$ are expanded into a set of hierarchical H_p-curl conforming basis functions, such as those proposed in [13, 14]:

$$\vec{E}\approx\sum_{i=1}^{N_p}e_i(t)\,\vec{f}_i(\vec{r}),\quad \vec{H}\approx\sum_{i=1}^{N_p}h_i(t)\,\vec{f}_i(\vec{r}), \quad (14)$$

where, $e_i(t)$ and $h_i(t)$ are unknown time-dependent coefficients weighting each basis functions. The test functions span an identical function space as the basis functions, leading to a Galerkin formulation. This leads to a set of coupled difference equations derived from (12) and (13) expressed as:

$$\mathbf{M}_{\mu}^{\mathbf{h},\mathbf{h}}\frac{\partial}{\partial t}\mathbf{h} + \mathbf{M}_{\sigma^{*}}^{\mathbf{h},\mathbf{h}}\mathbf{h} + \mathbf{S}^{\mathbf{h},\mathbf{e}}\mathbf{e} = -\mathbf{T}_M^{\mathbf{h}} - \mathbf{F}_E^{\mathbf{h},\mathbf{e}^{+}}\mathbf{e}^{+}, \quad (15)$$

$$\mathbf{M}_{\varepsilon}^{\mathbf{e},\mathbf{e}}\frac{\partial}{\partial t}\mathbf{e} + \mathbf{M}_{\sigma}^{\mathbf{e},\mathbf{e}}\mathbf{e} - \mathbf{S}^{\mathbf{e},\mathbf{h}}\mathbf{h} = -\mathbf{T}_J^{\mathbf{e}} + \mathbf{F}_H^{\mathbf{e},\mathbf{h}^{+}}\mathbf{h}^{+}, \quad (16)$$

where, the superscript **x,y** implies the **x**-field test function and **y**-field basis function, and **h** and **e** are the vectors of time-dependent coefficients $h_i(t)$ and $e_i(t)$. The vectors $\mathbf{h}^{+}$ and $\mathbf{e}^{+}$ are the coefficient vectors associated with exterior tangential fields from a coupled region. The matrix entries are computed as:

$$\left[\mathbf{M}_{\nu}\right]_{j,i} = \int_{V_i}\vec{f}_j\cdot\bar{\bar{\nu}}\cdot\vec{f}_i dv, \quad (17)$$

$$\left[\mathbf{S}\right]_{j,i} = \frac{1}{2}\int_{V_i}\left(\vec{f}_j\cdot\nabla\times\vec{f}_i + \vec{f}_i\cdot\nabla\times\vec{f}_j\right)dv, \quad (18)$$

$$\left[\mathbf{F}_{E/H}^{+}\right]_{j,k} = \frac{1}{2}\oint_{\partial V_i}\vec{f}_j\cdot\hat{n}_i\times\vec{f}_k^{+}ds, \quad (19)$$

$$\left[\mathbf{T}_J\right]_j = \int_{V_i}\vec{f}_j\cdot\vec{J}_V dv,\ \text{or}\ \left[\mathbf{T}_J\right]_j = -\frac{1}{2}\oint_{\partial V_i}\vec{f}_j\cdot\vec{J}_s ds, \quad (20)$$

where, $\vec{f}_i$ and $\vec{f}_j$ are the basis and testing functions, respectively, for the appropriate e-field or h-field, and $\bar{\bar{\nu}} = \bar{\bar{\mu}}, \bar{\bar{\varepsilon}}$, or $\bar{\bar{\sigma}}$. The **S** matrices have the property $\mathbf{S}^{\mathbf{h},\mathbf{e}} = \mathbf{S}^{\mathbf{e},\mathbf{h}^T}$. The matrices **M** are symmetric for isotropic media, and for rotationally symmetric anisotropic media.

The "face" matrices $\mathbf{F}_E^{\mathbf{h},\mathbf{e}^{+}}$ or $\mathbf{F}_H^{\mathbf{e},\mathbf{h}^{+}}$ represent the coupling to the neighboring sub-domains. The operator involves only the tangential projections of

the interior and exterior fields. Thus, when using curl-conforming basis functions, only the basis functions associated with the boundary topology (e.g., function spaces associated with faces and edges on ∂V_i) with overlapping support, contribute to these matrices. Consequently, the matrices are highly sparse. If the topology of the mesh on either side of ∂V_i are aligned (that is the faces and edges between the two sub-domains are shared), then $\mathbf{F}_E^{\mathbf{h},\mathbf{e}^+} = -\mathbf{F}_H^{\mathbf{e},\mathbf{h}^+}$. In general, the meshes need not align, and only the overlapping support of the vector basis functions on ∂V_i contribute to the face matrices.

The coupled equations in (15) and (16) are combined into a single difference equation as:

$$\dot{\mathbf{x}} = \mathbf{A}\mathbf{x} + \mathbf{B}\mathbf{x}^+ + \mathbf{t}, \tag{21}$$

where

$$\mathbf{x} = \begin{pmatrix} \mathbf{h} \\ \mathbf{e} \end{pmatrix}, \quad \mathbf{x}^+ = \begin{pmatrix} \mathbf{h}^+ \\ \mathbf{e}^+ \end{pmatrix}, \tag{22}$$

$$\mathbf{A} = \begin{pmatrix} -\mathbf{M}_\mu^{\mathbf{h},\mathbf{h}^{-1}}\mathbf{M}_{\sigma^*}^{\mathbf{h},\mathbf{h}} & -\mathbf{M}_\mu^{\mathbf{h},\mathbf{h}^{-1}}\mathbf{S}^{\mathbf{h},\mathbf{e}} \\ \mathbf{M}_\varepsilon^{\mathbf{e},\mathbf{e}^{-1}}\mathbf{S}^{\mathbf{e},\mathbf{h}} & -\mathbf{M}_\varepsilon^{\mathbf{e},\mathbf{e}^{-1}}\mathbf{M}_\sigma^{\mathbf{e},\mathbf{e}} \end{pmatrix}, \tag{23}$$

$$\mathbf{B} = \begin{pmatrix} 0 & -\mathbf{M}_\mu^{\mathbf{h},\mathbf{h}^{-1}}\mathbf{F}_E^{\mathbf{h},\mathbf{e}^+} \\ \mathbf{M}_\varepsilon^{\mathbf{e},\mathbf{e}^{-1}}\mathbf{F}_H^{\mathbf{e},\mathbf{h}^+} & 0 \end{pmatrix}, \tag{24}$$

$$\mathbf{t} = \begin{pmatrix} -\mathbf{M}_\mu^{\mathbf{h},\mathbf{h}^{-1}}\mathbf{T}_M^{\mathbf{h}} \\ -\mathbf{M}_\varepsilon^{\mathbf{e},\mathbf{e}^{-1}}\mathbf{T}_J^{\mathbf{e}} \end{pmatrix}. \tag{25}$$

The local difference equation (21), represents the first-order coupled differential equation for the fields in each sub-domain. The difference operators in all sub-domains are then solved simultaneously using a high-order Runge-Kutta (RK) scheme [2], [21]. It is noted that the local difference operator is implicit. That is, it involves the inversion of the matrix **M.** However, this local linear system is generally quite small, and this can be efficiently performed using an LU-factorization. The global linear system of equations, which consists of the combination of all the local linear systems, is thus an explicit formulation. The global system is conditionally stable. To date, an analytical study of the stability criterion has not been completed. However, via a heuristic analysis, a general stability criterion has been determined, which is expressed as:

$$c_o \Delta t \le \min \begin{cases} \left(\dfrac{h}{2}\sqrt{\varepsilon_r \mu_r}\, \dfrac{1}{(p+1)^2} \right), \text{hexahedron} \\ \left(\dfrac{h}{4}\sqrt{\varepsilon_r \mu_r}\, \dfrac{1}{(p+1)^2} \right), \text{tetrahedron} \end{cases} \tag{26}$$

where, h is the edge length, and p is the order of the H_p curl conforming basis (e.g, H_0 basis are the classic Whitney curl-conforming vector basis functions). Consequently, the stability criterion is based on the minimum edge length in the mesh. It is noted that through experimentation, this stability limit has been dependable, even for elements with very poor aspect ratios, and very small Jacobians.

IV. BOUNDARY CONDITIONS

On perfectly electrical conducting boundaries (PEC), the tangential electric field is presumed to be zero. Consequently, the curl-conforming basis associated with all edges and faces on a PEC surface are constrained to be zero. Similarly, $\vec{E}^+$ and $\vec{M}_s$ = 0 on the PEC boundary. Since $\vec{T}^e$ spans the same space as the electric field, the test functions on the PEC surface are also constrained to be zero. Thus, the right-hand-side of (13) also has null contribution on a PEC surface. Note that if the conductor is infinitesimally thin, distinct meshes on either side of the conductor must be assumed, so that the magnetic field on either side of the conductor is distinct. If the sub-domains boundaries are defined on the thin PEC surface, this is implicitly constrained by the DGFETD formulation.

A dual formulation is used to constrain the function space on the surface of a perfectly magnetic conductor (PMC) boundary. An impressed surface current density can also be placed on an exterior or an interior boundary. Surface currents couple directly into the sub-domains through the boundary terms in (12) and (13). The current density can be on the exterior boundary $\partial\Omega$, such as demanded by a hybrid modal/FEM or Boundary Element/FEM formulation. In this case, the exterior tangential fields $\hat{n}\times\vec{E}^+$ and $\hat{n}\times\vec{H}^+$ are assumed to be zero, since they are effectively represented by the current densities.

The surface current density can also lie within Ω on a sub-domain boundary ∂V_i. In this case, $\hat{n}\times\vec{E}^+$ and $\hat{n}\times\vec{H}^+$ would represent the exterior fields of the neighboring subdomain, and $\vec{M}_s$ and $\vec{J}_s$ the impressed current densities. It is noted that the step discontinuity in the fields are naturally represented by the DGFETD formulation.

An alternative source is a discrete lumped source model, such as a voltage source, current source, or discrete circuit mode (with internal impedance). To describe the implementation of such sources, we will begin with the simplest case,

which is a discrete voltage source, as illustrated in Fig. 1. The source is applied across a gap in a conductor path as represented by the shaded region on the left figure in Fig. 1. The gap has a length *g* along the unit axial vector of the gap, $\hat{g}$. If the gap is small relative to a wavelength, then the electric field in the gap can assumed to be constant, and is expressed as:

$$\vec{E}_g^{tot}(t) = \hat{g}\frac{V_s(t)}{g}\delta(g), \tag{27}$$

where, $V_s(t)$ is the time-dependent voltage. This can be incorporated into the finite element method by assuming that source gap field located on an edge of the mesh perpendicular to the gap axis. Then, from (12)

$$\begin{aligned}&\int_{V_i}\left[\frac{\partial}{\partial t}\vec{T}^h\cdot\vec{\bar{\mu}}\cdot\vec{H}+\vec{T}^h\cdot\vec{M}_V\right]dv+\\&\int_{V_i}\left[\frac{1}{2}\vec{T}^h\cdot\nabla\times\vec{E}+\frac{1}{2}\vec{E}\cdot\nabla\times\vec{T}^h\right]dv,\\&=-\frac{1}{2}\oint_{\partial V_i}\vec{T}^h\cdot\hat{n}\times\vec{E}_g^{tot}ds\end{aligned} \tag{28}$$

where, $\hat{n}$ is the unit normal directed out of V_i. (Note, the conductivity is assumed to be zero for simplicity). The surface integral is thus non-zero when tested with the edge basis $\vec{T}^h$ associated with the gap edge. It is further noted, that on the conductor, $\hat{n}\times\vec{E}$ and $\hat{n}\times\vec{T}^e = 0$.

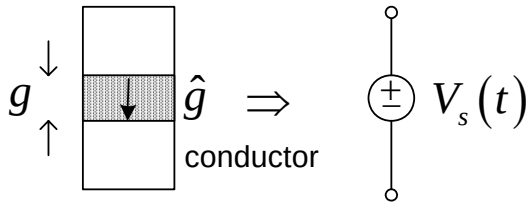

Fig. 1. Discrete voltage source model.

V. PML ABSORBING MEDIA

When simulating unbounded media, the FETD domain must be truncated and an exterior radiation boundary condition must be introduced on the truncation boundary. A number of approximate local absorbing boundary conditions could be employed [22]. However, such boundary conditions have limited accuracy, and require that the truncation boundary be placed a non-trivial distance from the device under test. Absorbing material layers have also been proposed to truncate the problem domain. The most accurate is the perfectly matched layer (PML) [23]. A number of PML formulations have been proposed for the DGTD method, including the anisotropic PML formulation[6, 8, 24], and a non-linear PML formulation [25]. In this paper, a PML formulation based on the stretched-coordinate formulation is presented [26, 27].

It is assumed that the extremity of the mesh is terminated by a PML media with Cartesian boundaries. Within the PML media, Maxwell's equations are expressed in a stretched coordinate form [26, 27]. The *x*-projections of Maxwell's equations in the frequency domain are then expressed as (note, a lossless anisotropic media is assumed for simplicity):

$$-j\omega\mu H_x = \frac{1}{s_y}\frac{\partial}{\partial y}E_z - \frac{1}{s_z}\frac{\partial}{\partial z}E_y, \tag{29}$$

$$j\omega\varepsilon\vec{E} = \frac{1}{s_y}\frac{\partial}{\partial y}H_z - \frac{1}{s_z}\frac{\partial}{\partial z}H_y, \tag{30}$$

where s_k ($k = x, y, z$) are the stretched coordinate metric coefficients [26]. The classical choice for the stretched coordinate coefficients is [28]:

$$s_k = \kappa_k + \frac{\sigma_k}{j\omega\varepsilon_o}, \quad k = x, y, z, \tag{31}$$

where κ_k and σ_k are assumed to be positive real, and can be one-dimensional functions along the *k*-direction. Starting with (29), both sides of the equation are multiplied by $s_y s_z$, leading to:

$$-j\omega\mu s_y s_z H_x = s_z\frac{\partial}{\partial y}E_z - s_y\frac{\partial}{\partial z}E_y. \tag{32}$$

Since, s_z and s_y are functions of *z* and *y* only, respectively, this can be re-written as:

$$-j\omega s_y s_z \mu H_x = \frac{\partial}{\partial y}s_z E_z - \frac{\partial}{\partial z}s_y E_y. \tag{33}$$

Defining the metric coefficients as in (31) leads to:

$$\begin{aligned}&-j\omega\left(\kappa_y+\frac{\sigma_y}{j\omega\varepsilon_o}\right)\left(\kappa_z+\frac{\sigma_z}{j\omega\varepsilon_o}\right)\mu H_x =\\&\frac{\partial}{\partial y}\left(\kappa_z+\frac{\sigma_z}{j\omega\varepsilon_o}\right)E_z - \frac{\partial}{\partial z}\left(\kappa_y+\frac{\sigma_y}{j\omega\varepsilon_o}\right)E_y\end{aligned}. \tag{34}$$

Next, the variable substitutions are made:

$$P_k^h = \frac{H_k}{j\omega}, \quad P_k^e = \frac{E_k}{j\omega}, \quad (k = x, y, z). \tag{35}$$

This substitution is applied to (34), leading to:

$$\begin{aligned}&-\left(j\omega\kappa_y\kappa_z+\frac{\left(\sigma_y\kappa_z+\sigma_z\kappa_y\right)}{\varepsilon_o}\right)\mu H_x - \frac{\sigma_y\sigma_z}{\varepsilon_o^2}\mu P_x^h\\&=\frac{\partial}{\partial y}\left(\kappa_z E_z+\frac{\sigma_z}{\varepsilon_o}P_z^e\right)-\frac{\partial}{\partial z}\left(\kappa_y E_y+\frac{\sigma_y}{\varepsilon_o}P_y^e\right)\end{aligned}. \tag{36}$$

A second variable substitution is made:

$$\begin{aligned}\tilde{H}_k &= \kappa_k H_k + \frac{\sigma_k}{\varepsilon_o} P_k^h, \\ \tilde{E}_k &= \kappa_k E_k + \frac{\sigma_k}{\varepsilon_o} P_k^e, \ (k = x, y, z)\end{aligned} . \quad (37)$$

This is substituted into (36), leading to:

$$-\mu \frac{1}{\kappa_x} \begin{pmatrix} j\omega\kappa_y\kappa_z \tilde{H}_x + \dfrac{\left(\sigma_y\kappa_z + \sigma_z\kappa_y\right)}{\varepsilon_o} \tilde{H}_x \\ -j\omega\kappa_y\kappa_z \dfrac{\sigma_x}{\varepsilon_o} P_x - \dfrac{\left(\sigma_y\kappa_z + \sigma_z\kappa_y\right)}{\varepsilon_o} \dfrac{\sigma_x}{\varepsilon_o} P_x \end{pmatrix} . \quad (38)$$

$$-\frac{\sigma_y\sigma_z}{\varepsilon_o^2}\mu P_x^h = \frac{\partial}{\partial y}\tilde{E}_z - \frac{\partial}{\partial z}\tilde{E}_y$$

From (35) and (37), it is further seen that:

$$j\omega P_x^h = H_x = \frac{1}{\kappa_x}\tilde{H}_x - \frac{1}{\kappa_x}\frac{\sigma_x}{\varepsilon_o} P_x . \quad (39)$$

Applying this to (38), leads to:

$$\begin{aligned} &-\left(j\omega\frac{\kappa_y\kappa_z}{\kappa_x} + \frac{\left(\sigma_y\kappa_z + \sigma_z\kappa_y\right)}{\kappa_x\varepsilon_o} - \frac{\kappa_y\kappa_z}{\kappa_x^2}\frac{\sigma_x}{\varepsilon_o} \right)\mu\tilde{H}_x \\ &-\left(\frac{\kappa_y\kappa_z}{\kappa_x^2}\frac{\sigma_x^2}{\varepsilon_o^2} + \frac{\sigma_y\sigma_z}{\varepsilon_o^2} - \frac{\sigma_x\left(\sigma_y\kappa_z + \sigma_z\kappa_y\right)}{\kappa_x\varepsilon_o^2} \right)\mu P_x \\ &= \frac{\partial}{\partial y}\tilde{E}_z - \frac{\partial}{\partial z}\tilde{E}_y . \end{aligned} \quad (40)$$

The expression in (40) can be written in the time-domain, and then generalized to all projections of Faraday's law as:

$$-\frac{\partial}{\partial t}\bar{\bar{a}}\cdot\mu\tilde{\vec{H}} - \bar{\bar{b}}\cdot\mu\tilde{\vec{H}} - \bar{\bar{c}}\cdot\mu\vec{P}^h = \nabla\times\tilde{\vec{E}} , \quad (41)$$

where, from (39)

$$\frac{\partial}{\partial t}\vec{P}^h = \bar{\bar{\kappa}}^{-1}\cdot\tilde{\vec{H}} - \bar{\bar{d}}\cdot\vec{P}^h . \quad (42)$$

The tensors $\bar{\bar{a}}, \bar{\bar{b}}, \bar{\bar{c}}, \bar{\bar{d}}$, and $\bar{\bar{\kappa}}$ are all diagonal tensors, defined by:

$$\begin{aligned} a_{xx} &= \frac{\kappa_y\kappa_z}{\kappa_x}, \\ b_{xx} &= \frac{1}{\kappa_x\varepsilon_o}\left(\sigma_y\kappa_z + \sigma_z\kappa_y - a_{xx}\sigma_x\right), \\ c_{xx} &= \frac{\sigma_y\sigma_z}{\varepsilon_o^2} - b_{xx}\frac{\sigma_x}{\varepsilon_o}, \\ d_{xx} &= \frac{\sigma_x}{\kappa_x\varepsilon_o}, \quad \kappa_{xx} = \kappa_x . \end{aligned} \quad (43)$$

The remaining diagonal terms of the tensors are derived via a permutation of the subscripts ($x \to y, y \to z, z \to x$).

A similar analogy is followed for Ampere's law, leading to the dual form:

$$+\frac{\partial}{\partial t}\varepsilon\bar{\bar{a}}\cdot\tilde{\vec{E}} + \varepsilon\bar{\bar{b}}\cdot\tilde{\vec{E}} + \varepsilon\bar{\bar{c}}\cdot\vec{P}^e = \nabla\times\tilde{\vec{H}} , \quad (44)$$

where, from (39)

$$\frac{\partial}{\partial t}\vec{P}^e = \bar{\bar{\kappa}}^{-1}\cdot\tilde{\vec{E}} - \bar{\bar{d}}\cdot\vec{P}^e . \quad (45)$$

In summary, the pertinent PML equations governing the fields in the PM region are given by (41), (42), (44), and (45). The unknowns in this region are thus $\tilde{E}$, $\tilde{H}$, $\tilde{P}^e$, and $\tilde{P}^h$.

It is observed that outside the PML region, $\bar{\bar{\kappa}} = \bar{\bar{a}} = \bar{\bar{I}}$, the unit dyad, and $\bar{\bar{b}} = \bar{\bar{c}} = \bar{\bar{d}} = 0$. Thus, outside the PML region $\tilde{H} = \vec{H}$ and $\tilde{E} = \vec{E}$, (41) and (44) reduce to the classical Maxwell curl equations, and (42) and (45) are not needed. Thus, $\vec{P}^e$, and $\vec{P}^h$ are only used in the PML region.

The PML region is also sub-divided into non-overlapping contiguous subdomains that are discretized with finite-elements. Within the discrete space, the field intensities and the auxiliary fields are expanded using H_p-curl conforming basis. Test functions that span an identical function space as the basis functions, are introduced. Following the procedure in (3) – (20), a Galerkin formulation is thus derived. This leads to the discrete linear operator:

$$\frac{\partial}{\partial t}\mathbf{M}_a^{\mathbf{h},\mathbf{h}}\mathbf{h} + \mathbf{M}_b^{\mathbf{h},\mathbf{h}}\mathbf{h} + \mathbf{M}_c^{\mathbf{h},\mathbf{h}}\mathbf{p}^{\mathbf{h}} + \mathbf{S}^{\mathbf{h},\mathbf{e}}\mathbf{e} + \mathbf{F}^{\mathbf{h},\mathbf{e}}\mathbf{e}^+ = 0 , \quad (46)$$

$$\frac{\partial}{\partial t}\mathbf{M}_a^{\mathbf{e},\mathbf{e}}\mathbf{e} + \mathbf{M}_b^{\mathbf{e},\mathbf{e}}\mathbf{e} + \mathbf{M}_c^{\mathbf{e},\mathbf{e}}\mathbf{p}^{\mathbf{e}} - \mathbf{S}^{\mathbf{e},\mathbf{h}}\mathbf{h} - \mathbf{F}^{\mathbf{e},\mathbf{h}}\mathbf{h}^+ = 0 , \quad (47)$$

$$\frac{\partial}{\partial t}\mathbf{M}^{\mathbf{h},\mathbf{h}}\mathbf{p}^{\mathbf{h}} - \mathbf{M}_{\kappa^{-1}}^{\mathbf{h},\mathbf{h}}\mathbf{h} + \mathbf{M}_d^{\mathbf{h},\mathbf{h}}\mathbf{p}^{\mathbf{h}} = 0 , \quad (48)$$

$$\frac{\partial}{\partial t}\mathbf{M}^{\mathbf{e},\mathbf{e}}\mathbf{p}^{\mathbf{e}} - \mathbf{M}_{\kappa^{-1}}^{\mathbf{e},\mathbf{e}}\mathbf{e} + \mathbf{M}_d^{\mathbf{e},\mathbf{e}}\mathbf{p}^{\mathbf{e}} = 0 , \quad (49)$$

where the matrices are defined in (17) – (19). Equations (46) – (49) can be expressed as a first order difference operator:

$$\dot{\tilde{\mathbf{x}}} = \mathbf{A}\tilde{\mathbf{x}} + \mathbf{B}\tilde{\mathbf{x}}^+ , \quad (50)$$

where,

$$\tilde{\mathbf{x}} = \begin{bmatrix} \tilde{\mathbf{h}} \\ \tilde{\mathbf{e}} \\ \mathbf{p}^h \\ \mathbf{p}^e \end{bmatrix}, \quad \tilde{\mathbf{x}}^+ = \begin{bmatrix} \tilde{\mathbf{h}}^+ \\ \tilde{\mathbf{e}}^+ \end{bmatrix}, \quad (51)$$

$$\mathbf{A} = \begin{bmatrix} -\mathbf{M}_a^{\mathbf{h},\mathbf{h}^{-1}}\mathbf{M}_b^{\mathbf{h},\mathbf{h}} & -\mathbf{M}_a^{\mathbf{h},\mathbf{h}^{-1}}\mathbf{S}^{\mathbf{h},\mathbf{e}} & -\mathbf{M}_a^{\mathbf{h},\mathbf{h}^{-1}}\mathbf{M}_c^{\mathbf{h},\mathbf{h}} & 0 \\ \mathbf{M}_a^{\mathbf{e},\mathbf{e}^{-1}}\mathbf{S}^{\mathbf{e},\mathbf{h}} & -\mathbf{M}_a^{\mathbf{e},\mathbf{e}^{-1}}\mathbf{M}_b^{\mathbf{e},\mathbf{e}} & 0 & -\mathbf{M}_a^{\mathbf{e},\mathbf{e}^{-1}}\mathbf{M}_c^{\mathbf{e},\mathbf{e}} \\ \mathbf{M}^{\mathbf{h},\mathbf{h}^{-1}}\mathbf{M}_\kappa^{\mathbf{h},\mathbf{h}} & 0 & -\mathbf{M}^{\mathbf{h},\mathbf{h}^{-1}}\mathbf{M}_d^{\mathbf{h},\mathbf{h}} & 0 \\ 0 & \mathbf{M}^{\mathbf{e},\mathbf{e}^{-1}}\mathbf{M}_\kappa^{\mathbf{e},\mathbf{e}} & 0 & -\mathbf{M}^{\mathbf{e},\mathbf{e}^{-1}}\mathbf{M}_d^{\mathbf{e},\mathbf{e}} \end{bmatrix} \quad (52)$$

$$\mathbf{B} = \begin{bmatrix} 0 & -\mathbf{M}_a^{\mathbf{h},\mathbf{h}^{-1}}\mathbf{F}^{\mathbf{h},\mathbf{e}} \\ \mathbf{M}_a^{\mathbf{e},\mathbf{e}^{-1}}\mathbf{F}^{\mathbf{e},\mathbf{h}} & 0 \end{bmatrix}. \qquad (53)$$

It is observed that with this form of the PML, arbitrary unstructured meshing can be employed within the PML region. The restriction is that the global PML *boundaries* be planar and orthogonal. It is further noticed that $\mathbf{p}^{\mathbf{h}}$ and $\mathbf{p}^{\mathbf{e}}$ are local to each subdomain and are not shared. Consequently, only the exterior fields $\tilde{\mathbf{h}}^+$ and $\tilde{\mathbf{e}}^+$ couple the sub-domains. It is further noted that when ∂V_i lies on the PML interface, $\tilde{\mathbf{h}}^+ = \mathbf{h}^+$, and $\tilde{\mathbf{e}}^+ = \mathbf{e}^+$. This is proven by observing in (37), that κ_k and σ_k are functions of *k*-only, and hence only impact the normal-projections of the fields on the PML boundaries. As a consequence, the mapped fields $\tilde{H}_k$ and $\tilde{E}_k$ maintain tangential continuity with the physical fields H_k and E_k.

VI. NUMERICAL STUDIES

The focus of this section is the validation of the DGFETD method presented in the previous sections. In the simulations presented, either three-dimensional hexahedral or tetrahedral meshes are used to discretize the volume. In all cases presented, the sub-domains V_i consist of a single finite element. The subdomain boundary ∂V_i is thus the faces of the polyhedron. In all cases, the sub-domain boundary faces are contiguous. Over each finite element, a variant of Webb's curl-conforming mixed-order hierarchal vector basis [14] were employed for tetrahedral elements. Hierarchal curl-conforming mixed-order basis functions for hexahedral elements have also been derived, and were used for hexahedral elements. RK-4 time-integration was used for all simulations for the time-integration of (21) and (50).

Initially, we consider the cavity resonator problem that is a PEC cube. The cube had a dimension of 1 m edge lengths. The fields within the cavity were excited by a volume current source randomly placed in the cavity. The time-dependent source had a differentiated Gaussian time-signature. The electric and magnetic fields were also probed during the time-simulation at a random location. The resonant frequencies of the cavity were extracted from the time-dependent fields using the FFT. The cavity was discretized with fitted hexahedral elements. The mesh densities ranged from 2 elements along an edge to 16 elements along an edge. The resonant frequencies were extracted for various order elements.

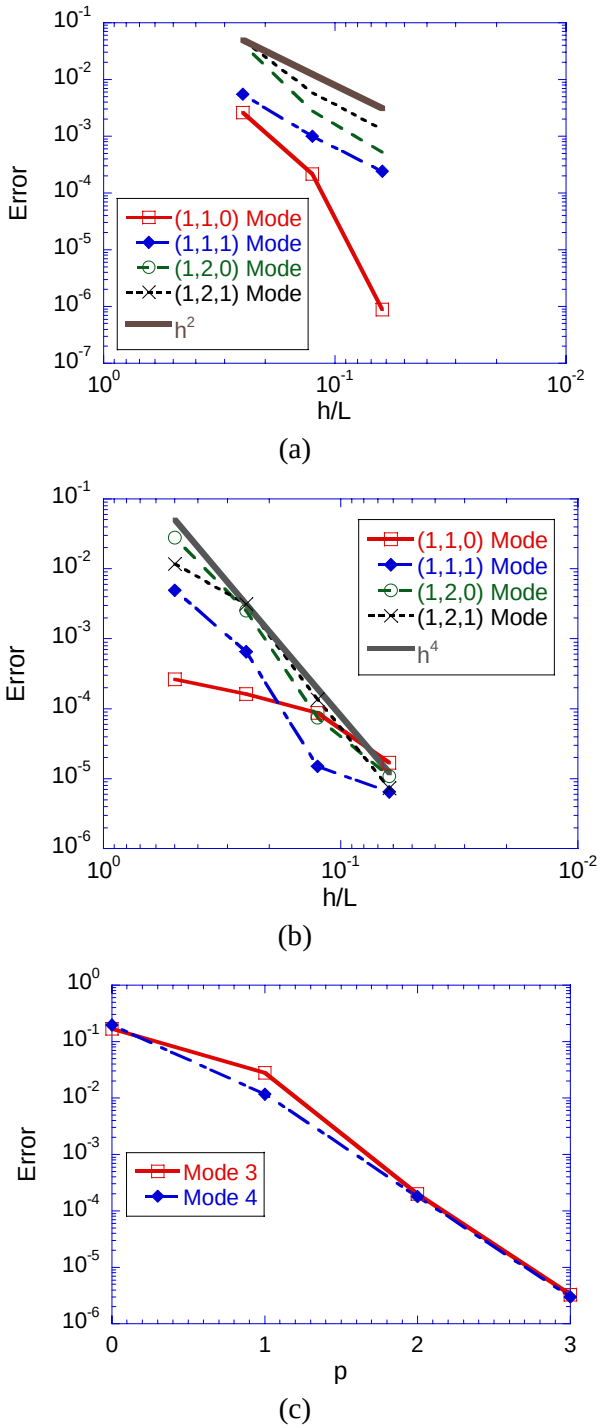

Fig. 2. Relative error for the first four modes of a 1 m PEC cube resonator. (a) H_0 basis, (b) H_1 basis, (c) varying basis order (h = 0.5 m).

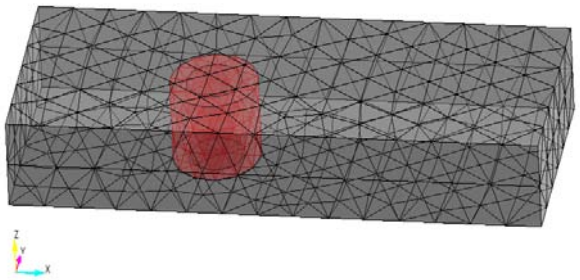

Fig. 3. Cavity ring resonator loaded with a dielectric ring tessellated with a quadratic tetrahedral mesh.

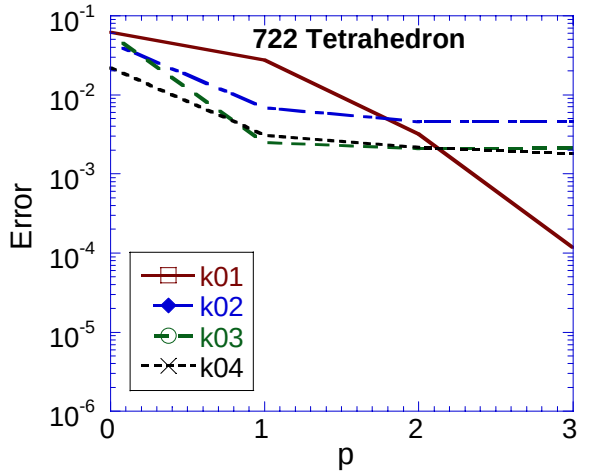

(a)

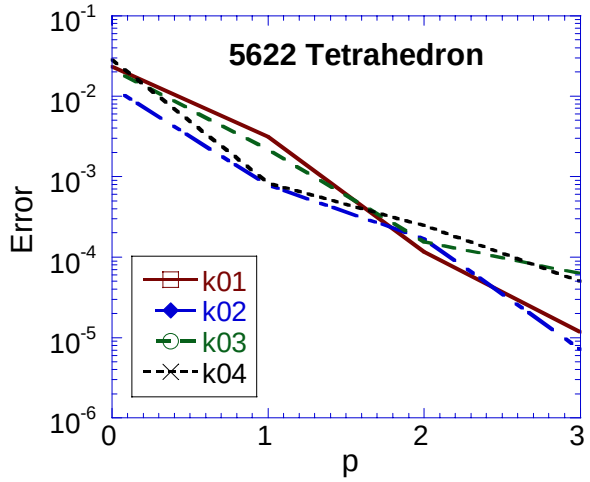

(b)

Fig. 4 Cavity ring resonator loaded with a dielec-tric ring tessellated with a quadratic tetrahedral mesh. (a) 722 quadratic tetrahedral mesh. (b) 5622 quadratic tetrahedral mesh.

Figures 2(a) and (b) illustrate the error of the first four modes in the cavity (the (1,1,0), (1,1,1), (1,2,0), and (1,2,1) modes, and their degenerate partners), as the mesh is refined for H_0 and H_1 basis functions. The error is expected to converge as $O(h^{2p})$ for the Galerkin procedure. Thus, a reference line is included. It is interesting to note that the (1,1,0) mode appears to super-converge. It is not clear why this is the case. Figure 2(c) illustrates the error in the predicted resonant frequency of the (1,2,0) and (1,2,1) modes for the coarsest mesh (2 elements on an edge) as the basis order is increased from p = 0 to 3. In each case, the error is observed to be converging as $O(h^{2p})$, as anticipated for the DGFETD method.

The next example studied is a cavity resonator loaded with a dielectric ring, as illustrated in Fig. 3 [29]. The rectangular PEC cavity has a dimension of 324 mm x 121 mm x 43 mm. The dielectric ring has an inner radius of 16.65 mm, and outer radious of 26.75 mm. The ring is sitting on the bottom of the cavity, but only has a height of 39 mm. The dielectric constant of the ring is 9.8. Again, the DGFETD method was used to extract the resonant frequencies of the loaded cavity. The cavity was excited in a similar manner as in the previous study.

The cavity was discretized with curvilinear second-order tetrahedron (10 nodes per tetrahedron). Here, two different meshes are presented. The first consisted of 722 quadratic tetrahedra. The second mesh consisted of 5,622 quadratic tetrahedra. (Note that curvilinear quadratic tetrahedra were used to more accurately resolve the ring geometry.) The basis function order was increased from p = 0 to 3 in each case. The error of the first 4 modes is presented in Figures (a) and (b) for the two meshes. A reference result was simulated using a denser mesh and high-order basis.

It is distinctly observed that for the coarse mesh, the error of the higher-order modes stagnate beyond p = 1. The reason for this is that the error is dominated by the boundary error of the surface of the dielectric ring. It appears that the lowest order mode is less dependent on the ring surface. The accuracy of the simulation could be improved by using higher-order tetrahedral elements. Unfortunately, such a meshing scheme was not available. Observing Fig. 4(b), the finer mesh leads to improved convergence to better than four digits of accuracy. If the basis order were increased further, the error will again stagnate due to the boundary error.

Table 1: Resonant frequencies of the PEC cavity loaded with the Dielectric ring as computed via the DSI, NFDTD, FETD, and DGFETD methods († reference [29])

Mode	DSI†	NFDTD†	FETD†	DGFETD
k01	0.952	0.952	0.9518	0.9518
k02	1.415	1.415	1.420	1.4151
k03	1.608	1.612	1.615	1.6109
k04	2.025	2.025	2.026	2.0257

Table 1 lists the resonant frequencies of the four modes to 5 digits calculated by the DGFETD method. As a reference, the resonant frequencies computed via the Discrete Surface Integral (DSI), the Non-Orthogonal FDTD (NFDTD), and a finite-element time-domain (FETD) method based on the vector wave equation are also provided. This data was obtained from [29].

The next set of problems involves unbounded domains that are terminated by the perfectly matched layer absorbing boundary condition. The first example is a parallel plate waveguide. The waveguide had PEC planes bounding the top and bottom boundaries. The side walls of the guide were PMC planes. The waveguide was discretized via rectangular hexahedron, which had 1 cm edge lengths. The waveguide was also meshed with tetrahedron with ~1 cm edge lengths.

The ends of the waveguide were terminated with PML layers. The TEM mode was excited in the guide via a surface current density. The time-dependent current had a Gaussian pulse time-signature with a 15 GHz bandwidth. The fields computed along the waveguide were Fourier transformed. The error of the phase and magnitude of the computed field relative to the exact field was computed. It is noted that the PML was tuned so that the PML reflection error was less than the computational error. Figure 5 (a) illustrates the maximum phase and magnitude error in the fields recorded over the frequency range of 0 to 15 GHz as a function of the order of the mixed-order curl-conforming basis functions. Typically, the maximum errors occurred at the highest frequencies. Exponential convergence of the solution is observed. It is noted that 6 digits of accuracy are realized for 4th order basis functions at this level of discretization. Figure 5 (b) illustrates the relative phase error for the tetrahedral mesh. This error is commensurate with that observed via the hexahedral mesh.

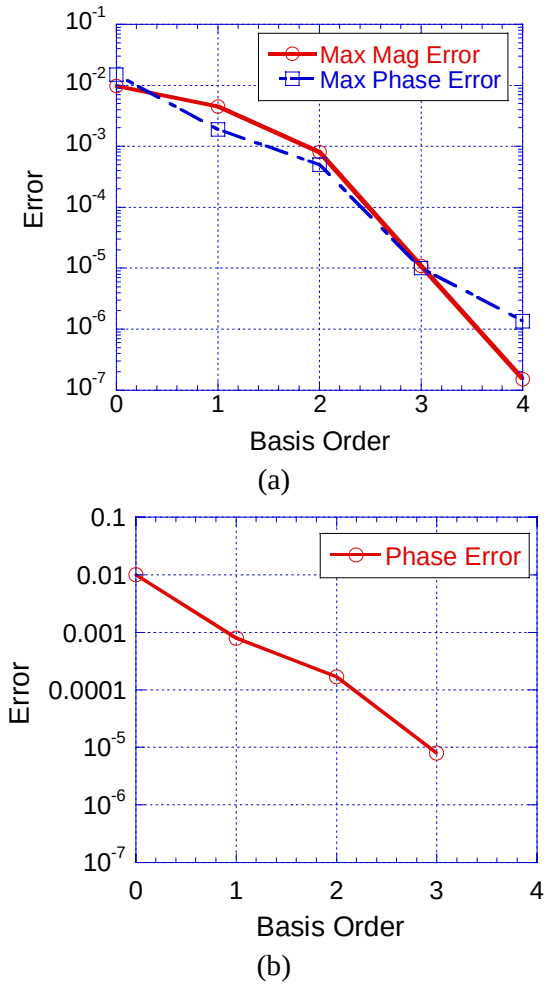

Fig. 5 Error in the electric field excited in a parallel plate waveguide discretized with (a) hexahedral, and (b) tetrahedral cells with 1 cm edge lengths. The maximum error over the 0 – 15 GHz frequency range is recorded as a function of the basis order.

Next, a more systematic study of the reflection error of the PML is presented. The parallel plate waveguide geometry is used again for this purpose. To extract the reflection error for the PML, a reference parallel plate waveguide was used that was sufficiently long so that the simulation would cease before reflections from the terminating boundary wall would return.

When applying the PML to FDTD applications, the PML is not actually perfectly matched since the discrete electric and magnetic fields are staggered in both space and time. As a consequence, the PML constitutive parameters must be spatially scaled to avoid large reflection errors. In the DGFETD formulation, the discrete electric and magnetic fields are co-located in both space and time. Thus, the PML is matched in the

discrete space. Discretization errors will still lead to reflection error. However, spatial scaling is not as imperative, and thinner PML layers can be used.

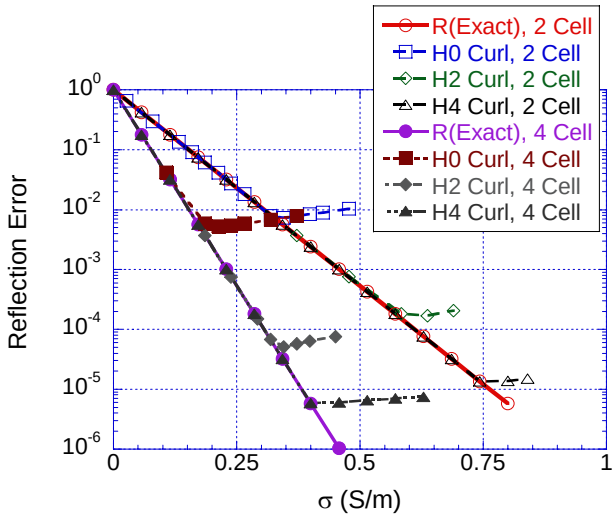

(a)

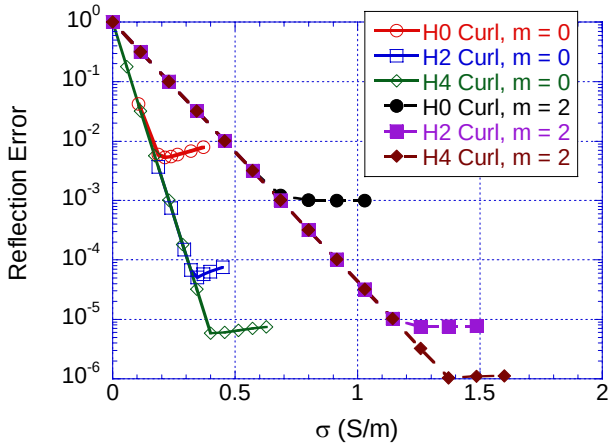

(b)

Fig. 6. Reflection error due to the PML termination of the parallel plate waveguide versus the PML conductivity ($\kappa = 1$) (a) for 2 and 4 cell thick PML layers with constant PML profile (m = 0), and (b) for a 4 cell thick PML with a polynomial scaled PML profile (m = 0, and m = 2).

The reflection error due to the PML as a function of the PML conductivity is presented in Fig. 6. The simulations used for Fig. 6 (a) assume PML parameters with a constant profile. Cases are presented where the PML was 2 and 4 hexahedral cells thick. H_0, H_2, and H_4 curl-conforming basis functions were employed. The exact reflection error is also illustrated in the plot, where

$$R(\text{Exact}) = e^{-2d\sigma\eta/(m+1)}, \qquad (54)$$

where, d is the thickness of the PML slab (in meters), σ is the normal PML conductivity, η is the free-space wave impedance, and m is the polynomial scaling factor of σ. The PML reflection error is dominated by the reflection error at the back PEC wall (namely, due to a round trip of the wave through the PML) for sufficiently small values of sigma. As sigma becomes sufficiently large, the reflection error levels off due to discretization error of the fields.

It is observed that increasing the basis order dramatically improves the reflection error. Though, it is also striking that increasing the thickness of the PML bears only a few dB improvement in the minimum reflection error. This implies that the bulk of the reflection error occurs at the PML interface boundary. In an attempt to improve this, σ is scaled using polynomial scaling [28]. Quadratic scaling is compared to a constant profile. It is found that this improves the reflection error by approximately 10 dB.

The final example is the extraction of the scattering parameters of a printed microstrip patch antenna printed on a dielectric substrate. The dimensions of the patch antenna are given in [30]. The antenna was simulated using both the FDTD method and the DGFETD method. The FDTD lattice was terminated with a tuned CFS-PML absorbing media [27, 28] that were 10 cells thick. The DGFETD mesh was terminated using the proposed PML scheme that were 2 cells thick. The FDTD simulations were performed with (65x60x17) lattice grid cells (FDTD(A)), and a refined mesh of (191x111x31) lattice grid cells. The DGFETD simulations were performed with 780 hexahedron and H_3 basis (DGFETD(A)), and with a finer discretization consisting of 3,120 hexahedron and H_2 basis (DGFETD(B)). A cross section of the mesh with 780 hexahedron is illustrated in Fig. 7. The microstrip line was excited by a soft current source placed under the microstrip. The line was matched via the PML boundary.

The magnitude of the reflection loss (S_{11}) is presented in Fig. 8 as computed by the FDTD and DGFETD methods each with two successive refinements. FDTD (A) has the most significant error. DGFETD(A) is also not yet converged.

There is good agreement with the finer FDTD and DGFETD discretizations.

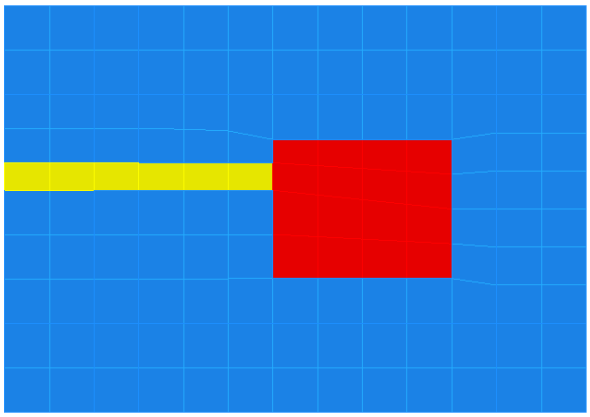

Fig. 7. Cross sectional view of the microstrip patch antenna fed by a microstrip line, discretized with the 780 cell hexahedral mesh.

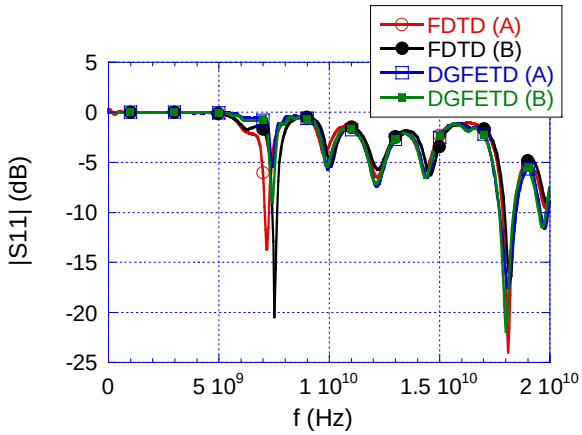

Fig. 8. Magnitude of scattering parameter S_{11} of the microstrip patch antenna computed via the FDTD method with lattice grids of dimension (A) (65x60x17) and (B) (191x111x31) lattice grid cells, and the DGFETD method with: (A) 780 hexahedron and H_3 basis and (B) 3,120 hexahedron and H_2 basis.

VII. CONCLUSIONS

A novel Discontinuous Galerkin Finite-Element Time-Domain (DGFETD) method has been presented in this paper. The DGFETD method is based on a spatial decomposition of the problem domain into non-overlapping sub-domains. A Galerkin formulation based on Maxwell's curl equations is imposed over each sub-domain. Each sub-domain is discretized independently using high-order hierarchal curl-conforming basis functions to discretize both the electric and the magnetic field intensities. The continuity of the fields across sub-domain boundaries is weakly enforced via boundary integral terms. By using curl-conforming basis, only basis functions associated with topologies that lie on the sub-domain boundary (i.e., face and edge basis functions) couple. The use of mixed-order curl-conforming basis avoids spurious solutions and the need for penalty methods.

The DGFETD method is a locally implicit/globally explicit method. That is, local to each sub-domain, a matrix inversion must be performed. However, since the sub-domains are generally quite small, this can be efficiently done via a LU-factorization. The global system of equations, which is superposition of all the sub-domains, is then solved via an explicit time-stepping algorithm. High-order Runge-Kutta (RK) schemes were used for this purpose.

For open region problems a perfectly matched layer (PML) absorbing boundary based on a stretched coordinate formulation was presented. PML absorbing layers have controllable accuracy, and are well suited for a high-order method. Since the electric and magnetic fields are co-located in both space and time, the scaling of the constitutive parameters is not necessary. In fact, reflection errors on the order of 0.001 % are possible with PML layers that are only 2 cells thick. However, it was shown that scaling the parameters can moderately reduce the reflection error.

Through numerical validation, it was demonstrated that the proposed DGFETD method does provide exponential convergence. It was also shown that the dispersion error can be dramatically reduced. This has great advantage when solving large scale problems, where phase errors are accumulated over long propagation distances. Unlike symplectic integration schemes, RK methods are also dissipative. However, it was also shown that the magnitude error is commensurate with the phase error, and the precision can be controlled via the high-order scheme.

Finally, since the DGFETD method is based on a spatial decomposition of the domain, and local solutions within these sub-domains, it is a naturally parallel algorithm. The most efficient parallel implementation of the algorithm is based on a distribution of sub-domains to processors based on contiguous non-overlapping domains of sub-domains. This will be the topic of a future publication.

REFERENCES

[1] B. Cockburn, G. E. Karniadakis, and C. W. Shu, *Discontinuous Galerkin Methods: Theory, Computation and Applications*, vol. 11. Berlin: Springer-Verlag Telos, 2000.

[2] M. H. Chen, B. Cockburn, and F. Reitich, "High-order RKDG methods for computational electromagnetics," *J. of Scientific Computing*, vol. 22 and 23, pp. 205-226, June 2005.

[3] J. S. Hesthaven, "High-order accurate methods in time-domain computational electromag-netics: A review," *Advances In Imaging And Electron Physics*, vol. 127, pp. 59-123, 2003.

[4] J. S. Hesthaven and T. Warburton, "Nodal high-order methods on unstructured grids - I. Time-domain solution of Maxwell's equations," *J. of Computational Physics*, vol. 181, pp. 186-211, 2002.

[5] J. S. Hesthaven and T. Warburton, "High-order nodal discontinuous Galerkin methods for the Maxwell eigenvalue problem," *Philosophical Trans. of The Royal Society of London Series A-Mathematical Physical And Engineering Sciences*, vol. 362, no. 1816, pp. 493-524, Mar 2004.

[6] T. Lu, P. W. Zhang, and W. Cai, "Discontinuous Galerkin methods for dispersive and lossy Maxwell's equations and PML boundary conditions," *J. of Computational Physics*, vol. 200, no. 2, pp. 549-580, Nov 2004.

[7] P. Monk and G. Richter, "A discontinuous Galerkin method for linear symmetric hyperbolic systems in inhomogeneous media," *J. of Scientific Computing*, vol. 22-23, no.1, 2005.

[8] T. Xiao and Q. H. Liu, "Three-dimensional unstructured-grid discontinuous Galerkin method for Maxwell's equations with well-posed perfectly matched layer," *Microwave Opt. Tech. Lett.*, vol. 46, no. 5, pp. 459-463, September 2005.

[9] L. F. Canino, J. J. Ottusch, M. A. Stalzer, J. L. Visher, and S. M. Wandzura, "Numerical solution of the Helmholtz equation in 2D and 3D using a high-order Nyström discretization," *J. of Computational Physics*, vol. 146, no. 2, pp. 627-663, 1998.

[10] S. D. Gedney, "On deriving a locally corrected Nyström scheme from a quadrature sampled moment method," *IEEE Trans. Antennas Propagat.*, vol. 51, no. 9, pp. 2402-2412, Sept. 2003.

[11] B. Cockburn, F. Y. Li, and C. W. Shu, "Locally divergence-free discontinuous Galerkin methods for the Maxwell equations," *J. Of Computational Physics*, vol. 194, no. 2, pp. 588-610, Mar 2004.

[12] S. Gedney, C. Luo, B. Guernsey, J. A. Roden, R. Crawford, and J. A. Miller, "The Discontinuous Galerkin Finite-Element Time-Domain Method (DGFETD): A High Order, Globally-Explicit Method for Parallel Computation," presented at *IEEE International Symposium on Electromagnetic Compatibility*, Honolulu, HI, 2007.

[13] D. K. Sun, J. F. Lee, and Z. Cendes, "Construction of nearly orthogonal Nedelec bases for rapid convergence with multilevel preconditioned solvers," *SIAM J. on Scientific Computing*, vol. 23, no. 4, pp. 1053-1076, 2001.

[14] J. P. Webb, "Hierarchical vector basis functions of arbitrary order for triangular and tetrahedral finite elements," *IEEE Trans. Antennas Propagat.*, vol. 47, no. 8, pp. 1244-1253, 1999.

[15] P. Fernandes and M. Raffetto, "Characterization of spurious-free finite element methods in electromagnetics," *Compel-The International Journal For Computation And Mathematics In Electrical And Electronic Engineering*, vol. 21, no. 1, pp. 147-164, 2002.

[16] J. S. Hesthaven and T. Warburton, "High-order accurate methods for time-domain electromagnetics," *CMES-Computer Modeling In Engineering & Sciences*, vol. 5, no. 5, pp. 395-407, May 2004.

[17] B. Donderici and F. L. Teixeira, "Mixed finite-element time-domain method for transient Maxwell equations in doubly dispersive media," *IEEE Trans. Micro. Theory Tech.*, vol. 56, no. 1, pp. 113-120, Jan 2008.

[18] R. N. Rieben, G. H. Rodrigue, and D. A. White, "A high order mixed vector finite element method for solving the time

dependent Maxwell equations on unstructured grids," *J. of Computational Physics*, vol. 204, no. 2, pp. 490-519, Apr 10 2005.

[19] R. Rieben, D. White, and G. Rodrigue, "High-order symplectic integration methods for finite element solutions to time dependent Maxwell equations," *IEEE Trans. Antennas Propagat.*, vol. 52, no. 8, pp. 2190-2195, Aug 2004.

[20] G. Rodrigue and D. White, "A vector finite element time-domain method for solving Maxwell's equations on unstructured hexahedral grids," *SIAM Journal On Scientific Computing*, vol. 23, no. 3, pp. 683-706, Oct 1 2001.

[21] S. Gottlieb, C. W. Shu, and E. Tadmor, "Strong stability-preserving high-order time discretization methods," *SIAM Review*, vol. 43, no. 1, pp. 89-112, 2001.

[22] J. Jin, *The Finite Element Method in Electromagnetics*. New York: John Wiley & Sons, Inc., 1993.

[23] J. P. Berenger, "A perfectly matched layer for the absorption of electromagnetic waves," *J. of Computational Physics*, vol. 114, no. 2, pp. 195-200, 1994.

[24] J. H. Lee and Q. F. Liu, "A 3-D spectral-element time-domain method for electromagnetic simulation," *IEEE Trans. Micro. Theory Tech.*, vol. 55, no. 5, pp. 983-991, May 2007.

[25] S. Abarbanel, D. Gottlieb, and J. S. Hesthaven, "Non-linear PML equations for time dependent electromagnetics in three dimensions," *J. Of Scientific Computing*, vol. 28, no. 2-3, pp. 125-137, Sep 2006.

[26] W. C. Chew and W. H. Weedon, "A 3D Perfectly Matched Medium from Modified Maxwells Equations with Stretched Coordinates," *Micro. Opt. Tech. Lett.*, vol. 7, no. 13, pp. 599-604, 1994.

[27] J. A. Roden and S. D. Gedney, "Convolutional PML (CPML): An Efficient FDTD Implementation of the CFS-PML for Arbitrary Media," *Micro. Opt. Tech. Lett.*, vol. 27, no.5, pp. 334-339, December 2000.

[28] S. D. Gedney, "Perfectly Matched Layer Absorbing Boundary Conditions," in *Computational Electrodynamics: The Finite-Difference Time-Domain Method*, A. Taflove and S. B. Hagness, Eds., 3rd ed. Boston: Artech House, 2005.

[29] S. D. Gedney and J. A. Roden, "Numerical stability of non-orthogonal FDTD methods," *IEEE Trans. Antennas Propagat.*, vol. 48, no. 2, pp. 231-239, 2000.

[30] D. M. Sheen, S. M. Ali, M. D. Abouzahra, and J. A. Kong, "Application of the three-dimensional finite-difference time-domain method to the analysis of planar microstrip circuits," *IEEE Trans. Micro. Theory Tech.*, vol. 38, no. 7, pp. 849-857, July 1990.

Stephen D. Gedney received the B.Eng.-Honors degree from McGill University, Montreal, P.Q., in 1985, and the M.S. and Ph.D. degrees in Electrical Engineering from the University of Illinois, Urbana-Champaign, IL, in 1987 and 1991, respectively. He is currently a Professor with the Department of Electrical and Computer Engineering at the University of Kentucky, where he has been since 1991. From 1985 to 1987, he worked for the U.S. Army Corps of Engineers, Champaign, IL. In the summers of 1992 and 1993 was a NASA/ASEE Faculty Fellow at the Jet Propulsion Laboratory, Pasadena, CA. In 1996 he was a visiting Professor at the Hughes Research Labs (now HRL laboratories) in Malibu, CA. He received the Tau Beta Pi Outstanding Teacher Award in 1995. In 2002, S. Gedney was named as the Reese Terry Professor of Electrical and Computer Engineering at the University of Kentucky. He is also a Fellow of the IEEE. Prof. Gedney's research is in the area of computational electromagnetics with focus in high-order solution techniques, fast solver technology, advanced time-domain methods, and parallel algorithms. His research has focused on applications in the areas of electromagnetic scattering and microwave circuit modeling and design.

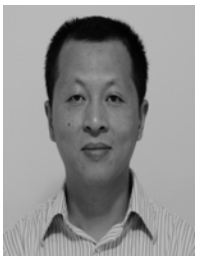

Chong Luo was born in Sichuan, China, in 1972. He received B.S. degree, in Electrical Engineering from Beijing University of Aeronautics and Astronautics, Beijing, China, in 1994, the M.S. and Ph.D. degrees in Electrical Engineering from University of Kentucky, Lexington, in May 2002 and December 2005. He is currently Alpha Omega Electromagnetics. His primary research interest is in computational electromagnetics. Dr. Luo is a member of IEEE.

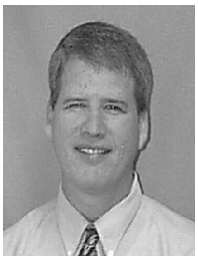

Alan Roden is a Senior Project Leader with The Aerospace Corporation where his responsibilities include electromagnetic analysis and design for satellite systems. Previously, Dr. Roden worked with The Georgia Tech Research Institute in Atlanta Georgia, and the IBM Corporation in Research Triangle Park, NC. He received his Ph.D. in Electrical Engineering from the University of Kentucky, Lexington, KY in 1997, his master's degree in electrical engineering from North Carolina State University in 1989, and his B.S. from the University of Tennessee at Chattanooga in 1984. Dr. Roden is a senior member of the IEEE and has published over 30 journal and conference papers.

Robert D. Crawford received a B.S. in Computer Science from the University of Illinois Urbana-Champaign in 1986 and an M.S. in Mathematics from Illinois State University in 1988. Mr. Crawford has been developing and managing the development of EM Simulation Software (both asymptotic and full-wave) for the past 8 years.

Bryan Guernsey graduated from Virginia Tech in 2005 with a BS in Electrical Engineering, 2007 from The University of Kentucky with a MSEE focusing in Computational Electromagnetics. He is currently working as a member of the technical staff for The Aerospace Corporation in Chantilly Va.

Jeffrey A. Miller received the BS, MS and PhD degrees in electrical engineering from Texas A&M University, College Station, in 1987, 1989, and 2001, respectively. Has has been employed by Texas Instruments, McKinney, TX, where he designed and analyzed broad-band antennas. He has also worked at Northrop Grumman, Pico Reivera, CA, in the area of low observable Technology. He is currently a Senior Engineering Specialist with the Aerospace Corporation, Chantilly, VA, where he specializes in antennas and electromagnetic analysis

Tyler C. Kramer (M'02) was born in Reading, PA. He obtained his BSEE and MSEE degrees from Virginia Tech in 2004 and 2007, respectively. From 2004 to 2005 he was employed as a Research Scientist at Nanosonic, Inc, Blacksburg VA. He is currently employed as a Member of the Technical Staff at The Aerospace Corporation, specializing in computational and applied electromagnetics.

Eric W. Lucas received the B.S. and M.S.E.E degrees from George Mason University, Fairfax, Va. In 1984 and 1989 respectively. In 1993, he received the Ph.D. degree from the University of Maryland, College Park under Professor Isaac Mayergoyz. In 1985 he joined the Microwave Branch of Harry Diamond Lab (Army Research Lab). In 1986 Dr. Lucas joined the Westinghouse (now Northrop Grumman) Antenna Aperture and Integrated Sensor Department, Baltimore MD. Dr. Lucas was a Fellow Engineer there, responsible for the development of wideband, wide-scanning low-observable phased array aperture technologies. In 1998 Dr. Lucas founded Alpha Omega Electromagnetics, LLC., a MD-based antenna and electromagnetic simulation software technology development firm. His research interests include diverse antenna technologies as well as state-of-the-art, industrial grade electromagnetic simulation software and algorithm development.